RSC Advances

PAPER

View Article Online
View Journal | View Issue

Cite this: *RSC Adv.*, 2017, **7**, 22454

Facile synthesis of NiS_2@MoS_2 core–shell nanospheres for effective enhancement in microwave absorption†

Xiao-Juan Zhang,‡[a] Shan-Wen Wang,‡[a] Guang-Sheng Wang,*[a] Zhen Li,*[b] Ao-Ping Guo,[a] Jia-Qiang Zhu,[a] Da-Peng Liu[a] and Peng-Gang Yin*[a]

Received 20th March 2017
Accepted 13th April 2017

DOI: 10.1039/c7ra03260a

rsc.li/rsc-advances

Core–shell structured NiS_2@MoS_2 nanospheres have been successfully fabricated *via* a facile hydrothermal method. The structure and morphology of the nanospheres were characterized by X-ray diffraction (XRD), X-ray photoelectron spectroscopy (XPS), scanning electron microscopy (SEM), field emission scanning electron microscopy (FESEM) and transmission electron microscopy (TEM). The results indicated that this unique core–shell structure was beneficial to high-performance microwave absorption. A possible absorption mechanism was explained in detail. As an absorber, nanocomposites with a filler loading of 20 wt% exhibited enhanced microwave absorption properties due to characteristic impedance matching, synergistic effects, dipole and interface polarization, multiple reflections and quarter-wavelength matching. The minimum reflection loss can reach −41.05 dB at 12.08 GHz, and the absorption bandwidth exceeding −10 dB is 4.4 GHz with a thickness of 2.2 mm.

Introduction

Nowadays, it is essential to exploit new and highly efficient microwave absorbers against electromagnetic (EM) radiation caused by electronic apparatus or radar systems, which will lead to undesirable EM pollution.[1–3] Significant effort has been devoted to designing enhanced microwave absorbers with different morphologies and structures.[4–6] Nanomaterials are attracting considerable attention in a variety of fields such as lithium-ion batteries,[7] supercapacitors,[8–10] energy storage,[11] and electrocatalysts for the oxygen reduction reaction and the hydrogen evolution reaction,[12,13] as well as EM wave absorbers due to their diverse structural types, abundant and inexpensive nature, especially for metal sulfides. To date, various metal sulfides such as MoS_2 nanosheets,[14] 3D MoS_2 nanospheres,[15] hierarchical CuS nanospheres,[16,17] CdS nanocrystals,[18] Bi_2S_3 nanorods[19] and CuS nanoflakes[20] have been utilized as EM wave absorbing materials.

As is well known, nano-structural engineering is beneficial to improving microwave absorption property. Recently, extensive studies have proved that a variety of nanomaterials with core–shell or yolk–shell structure can be used as high-performance microwave absorbers due to the synergistic effects of both the cores and shells. Compared to single type of wave absorber, multi-components always exhibit much stronger reflection loss. For example, Xu *et al.*[21] investigated the microwave absorption performance of ellipsoidal Fe_3O_4@$CuSiO_3$ nanorattles with different aspect ratios. Because of the strong magnetic loss and improvement of dielectric loss, they exhibited enhanced microwave absorption property with a minimum reflection loss of −30.8 dB at 8.0 GHz. Liu *et al.*[4] fabricated CoNi@SiO_2 core–shell, CoNi@SiO_2@TiO_2 core–shell–shell and CoNi@Air@TiO_2 yolk–shell microspheres in a facile process and investigated their microwave absorption properties, respectively. The results showed that the CoNi@SiO_2@TiO_2 absorbers exhibited the most enhanced microwave absorption ability. In addition, the research about hierarchical Fe_3O_4@TiO_2 yolk–shell microspheres,[22] yolk–shell C@C microspheres,[23] $FeSn_2$/Sn/graphite core–shell nanoparticles,[24] yolk–shell Fe_3O_4@ZrO_2 structure,[25] double-shelled Fe_3O_4@SnO_2 yolk–shell microspheres,[26] Fe_3O_4/C core–shell nanospindles,[27] Ni@TiO_2 and Ni@SiO_2 core–shell microspheres[28] *et al.* has further verified that the core–shell or yolk–shell structure is beneficial to obtaining higher microwave absorption performance.

As for these core–shell or yolk–shell structural wave absorbers, the agglomeration of magnetic core or complicated preparation method restricts their practical application immensely. In order to solve these problems, using metal sulfides is more promising for EM wave absorption property on account of their typical dielectric loss mechanism. Furthermore, reports on core–shell nanostructural wave absorbers

[a]*School of Chemistry and Environment, Key Laboratory of Bio-Inspired Smart Interfacial Science and Technology of Ministry of Education, Beihang University, Beijing 100191, P. R. China. E-mail: wanggsh@buaa.edu.cn; pgyin@buaa.edu.cn*

[b]*Changjiang River Scientific Research Institute of Changjiang Water Resources Commission, Wuhan, Hubei Province, 430010, P. R. China. E-mail: 951419476@qq.com*

† Electronic supplementary information (ESI) available. See DOI: 10.1039/c7ra03260a

‡ Xiao-Juan Zhang and Shan-Wen Wang are co-first authors.

composed of transition metal sulfides are still scarce. Based on this, we demonstrate the successful design and fabrication of uniform core–shell NiS_2@MoS_2 microspheres through a facile hydrothermal route with enhanced microwave absorption performance for the first time. As expected, the synthesized NiS_2@MoS_2 microspheres exhibits excellent wave absorption property compared with that of single NiS_2 or MoS_2 nanomaterial.

Results and discussion

As shown in Scheme 1, the NiS_2 nanospheres have been fabricated by a simple solvothermal method. After that, the NiS_2 nanospheres could play the role of nucleation site for MoS_2. The generated MoS_2 nanoplates coated on the surface of NiS_2 nanospheres due to the strong affinity which caused by homologous inorganic molecules between the nucleation sites and MoS_2 nanoplates to form core–shell structural NiS_2@MoS_2 nanospheres. The wrinkled nanoplates would increase the specific surface area that is beneficial to obtain higher microwave absorption performance.

In order to study the crystal structure of NiS_2 and NiS_2@MoS_2 nanospheres, the XRD patterns have been provided in Fig. 1a. It can be seen that all the diffraction peaks are readily indexed to the cubic vaesite (JCPDS no. 11-0099). The narrow sharp peaks confirm that the material should be highly crystallized NiS_2 without any other impurities. In addition, the XRD pattern of NiS_2@MoS_2 nanospheres is almost the same as that of NiS_2 nanospheres, while the intensity of peaks become weaker due to the coated MoS_2 nanoplate. The XRD pattern of MoS_2 nanoplate shown in Fig. S1† indicates that the MoS_2 nanoplate is weak crystalline and the intensity of peaks is far lower than that of NiS_2 nanospheres. As a result, the XRD peaks of MoS_2 nanoplate cannot be displayed in the pattern of NiS_2@MoS_2 nanospheres. To verify the existence of MoS_2, the surface chemical states of NiS_2@MoS_2 nanospheres are further investigated *via* the X-ray photoelectron spectroscopy (XPS). The core level of the Ni 2p spectrum shown in Fig. 1b can be deconvoluted into two spin–orbit doublets. The peaks at 857.37 and 875.38 eV are attributed to $2p_{3/2}$ and $2p_{1/2}$ of Ni^{2+}, and the peaks at 861.67 and 880.38 eV are assigned to $2p_{3/2}$ and $2p_{1/2}$ of Ni^{3+}, respectively. The existence of Ni^{3+} is mainly due to the slight oxidation of NiS_2 on the surface.[29] From the Mo 3d spectrum, it certainly turns out that the Mo atom exists as +4

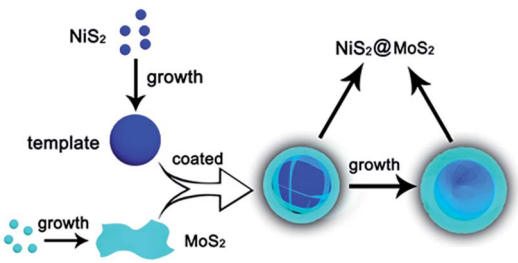

Scheme 1 Schematic illustration of the synthetic procedure for the NiS_2@MoS_2 nanospheres.

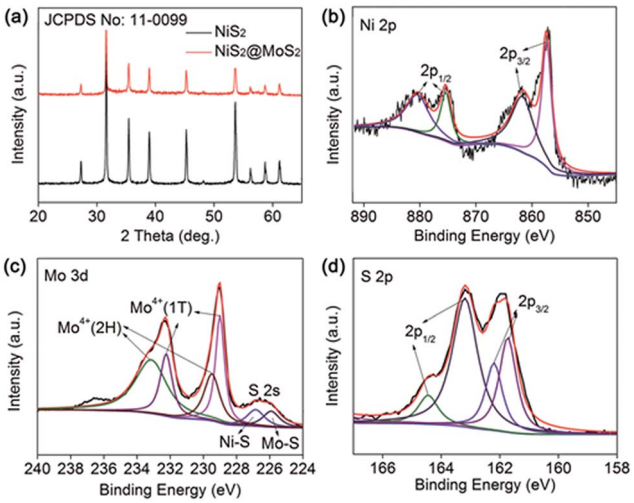

Fig. 1 (a) XRD pattern of NiS_2 and NiS_2@MoS_2 nanospheres; XPS spectra of (b) Ni 2p, (c) Mo 3d, (d) S 2p.

oxidation state. The two peaks at 233.12 eV (Mo^{4+} $3d_{3/2}$) and 229.46 eV (Mo^{4+} $3d_{5/2}$) are from the semiconducting 2H-phase MoS_2, and those at 232.22 eV (Mo^{4+} $3d_{3/2}$) and 228.98 eV (Mo^{4+} $3d_{5/2}$) are assigned to metallic 1T-phase MoS_2.[30] In addition, the nearby S 2s peaks are deconvoluted into two peaks at 226.83 and 225.90 eV, corresponding to the two chemical states of S species bonding with Ni and Mo ions (Fig. 1c). For the S 2p spectra (Fig. 1d), the XPS peak is deconvoluted into four peaks. The peaks at 164.45 and 162.19 eV are assigned to the S $2p_{1/2}$ and S $2p_{3/2}$ orbitals of divalent sulfide ions (S^{2-}) in MoS_2, while the other two peaks at 163.18 and 161.71 eV are attributed to S $2p_{1/2}$ and S $2p_{3/2}$ of Ni–S bondings. Therefore, the XPS characterization have indicated the successful synthesis of NiS_2@MoS_2 core–shell nanostructures and suggested a strong interaction between these two phases.[31]

The sizes and morphologies of the as-synthesized NiS_2 and NiS_2@MoS_2 nanospheres were characterized by SEM and TEM. An overview of SEM images (Fig. 2a and b) show the surface

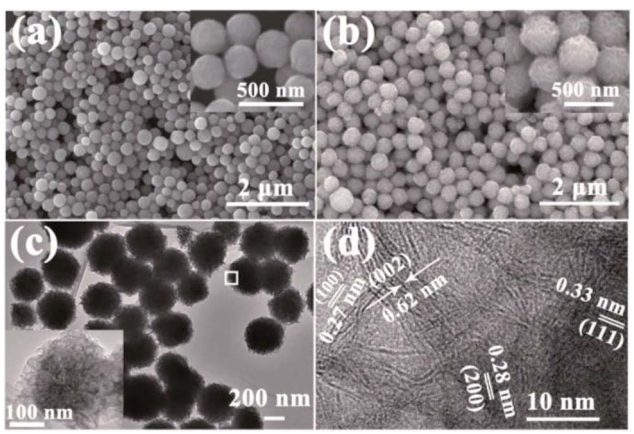

Fig. 2 SEM images of (a) NiS_2 and (b) NiS_2@MoS_2 nanospheres. Inset: magnified SEM images; (c) TEM image; (d) high-resolution TEM image of NiS_2@MoS_2 nanospheres.

morphology, indicating that the particles exhibit uniform nanospheres with smooth or wrinkled surface. A magnified SEM images insetted in Fig. 2a and b reveal that the average diameter of these two samples are about in the range of 200–250 nm and 250–300 nm. To verify the core–shell structure of NiS_2@MoS_2 nanospheres, the TEM and HRTEM images have been provided in Fig. 2c and d. From the TEM image, it is obviously seen that the solid sphere as core and the curved nanoplates as shell. And the nanoplate-assembled layer is about 25 nm. As shown in Fig. 2d, the ordered lattice fringes are clearly observed from a high-resolution TEM image. The spacings between two neighboring lattice fringes are approximately 0.62 nm and 0.27 nm, corresponding to the (002) and (100) plane of MoS_2 shell. Then for NiS_2 core, the spacings between two neighboring lattice fringes are approximately 0.33 nm and 0.28 nm, corresponding to the (111) and (200) plane, respectively. Moreover, the FESEM images of NiS_2@MoS_2 nanospheres presented in Fig. S2† reveal the NiS_2 core and MoS_2 shell explicitly.

To further illuminate the core–shell structure of NiS_2@MoS_2 nanospheres, the FESEM characterization and the corresponding elemental maps have been displayed in Fig. 3. In the rectangular region, the elemental maps of S, Ni and Mo demonstrate that the NiS_2@MoS_2 nanospheres are composed of NiS_2 core and MoS_2 shell indeed. Moreover, as shown in Fig. S3,† the elemental mapping of S, Ni and Mo elements in line-scanning mode and atomic percent correspond to this result. The unique structure is helpful for the high-efficiency electromagnetic-wave absorption property.

It is very interesting that the coated state will become very different with variable quantity of sodium molybdate and L-cysteine. As shown in Fig. 4, when the amount of sodium molybdate and L-cysteine decrease to half of the original (0.04 g and 0.08 g), only a little nanoplate coated on the surface of NiS_2 nanospheres. On the other hand, when their amounts increase twice compared to the original amount (0.16 g and 0.32 g), much redundant MoS_2 nanoplates generate. These results indicate that, with proper control of the relative ratios of sodium molybdate to NiS_2 nanospheres, core–shell structural NiS_2@MoS_2 nanospheres can be successfully fabricated.

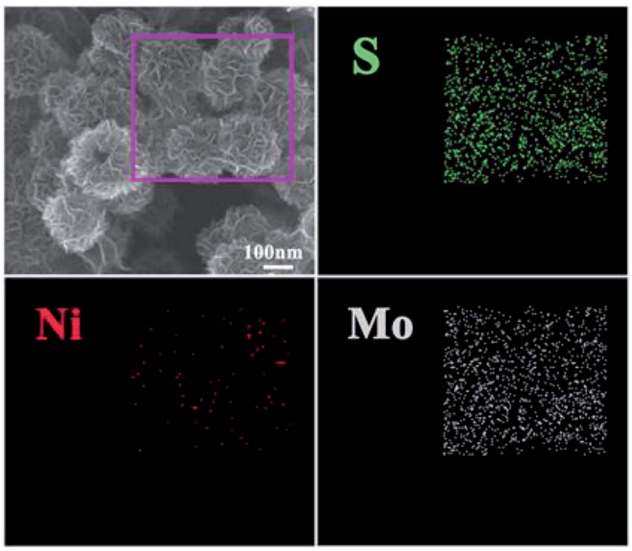

Fig. 3 FESEM image of the NiS_2@MoS_2 nanospheres and corresponding elemental mapping images of S, Ni and Mo.

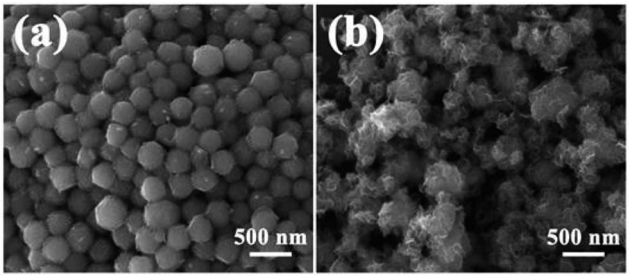

Fig. 4 FESEM images of NiS_2@MoS_2 samples under different conditions: (a) $Na_2MoO_4 \cdot 2H_2O$: 0.04 g, L-cysteine: 0.08 g; (b) $Na_2MoO_4 \cdot 2H_2O$: 0.16 g, L-cysteine: 0.32 g.

The electromagnetic wave absorption properties of NiS_2 and NiS_2@MoS_2 nanospheres are investigated in terms of reflection loss. According to the transmission line theory, the reflection loss (RL) values are calculated using the measured data of relative permittivity and permeability at a given frequency and thickness layer, which is summarized by the following equations:[32]

$$z_{in} = \sqrt{\frac{\mu_r}{\varepsilon_r}} \tanh\left[j\left(\frac{2f\pi d}{c}\right)\sqrt{\mu_r \varepsilon_r}\right] \quad (1)$$

$$RL = 20 \log\left|\frac{Z_{in} - Z_0}{Z_{in} + Z_0}\right| \quad (2)$$

where, ε_r and μ_r (for NiS_2 and NiS_2@MoS_2, μ_r is thought as 1) are the complex permittivity and permeability of the composite absorber, respectively; f is the frequency; d is the thickness of the absorber, and c is the velocity of light in free space; Z_{in} is the input characteristic impedance, Z_0 is the impedance of free space. Fig. 5a shows the RLs of MoS_2/PVDF, NiS_2/PVDF and NiS_2@MoS_2/PVDF with different loadings at a thickness of 2.2 mm. It is found that the minimum RL value of NiS_2@MoS_2/PVDF with 20 wt% loading decreases rapidly to −41.05 dB at 12.08 GHz, whereas that of MoS_2/PVDF and NiS_2/PVDF are −12.47 dB at 15.52 GHz and −15.40 dB at 14.40 GHz under the same loadings. As for NiS_2@MoS_2/PVDF, when the filler loading decreased to 10 wt% or increased to 30 wt%, the minimum RL value is far less than that of 20 wt%, indicating that the optimum loading is 20 wt%. As shown in Fig. S4,† the RL value of NiS_2@MoS_2/PVDF with 20 wt% loading varies with the thickness. In addition, NiS_2@MoS_2/PVDF with 20 wt% loading exhibits a wide frequency bandwidth of effective attenuation (RL < −10 dB) up to 4.40 GHz (10.16–14.56 GHz). Fig. 5b–d show three dimensional plots of calculated theoretical RLs of NiS_2@MoS_2/PVDF *versus* the frequency and thickness at different loadings. This indicates the microwave absorption property at different frequencies can be tuned greatly by controlling the thickness and the filler contents of the absorbers.

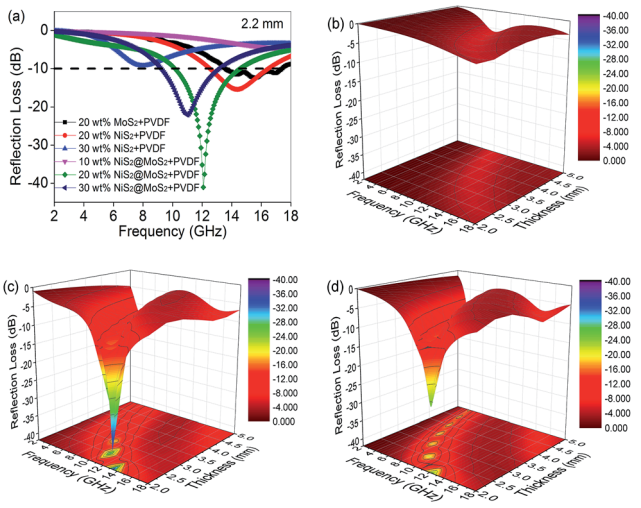

Fig. 5 (a) Microwave RL curves of the composites with a thickness of 2.2 mm in the frequency range of 2–18 GHz. Three-dimensional representations of the RL of NiS_2@MoS_2/PVDF composites with a filler loading of (b) 10 wt%, (c) 20 wt% and (d) 30 wt%.

It is well-known that the electromagnetic wave absorption performance is closely correlated with their complex relative permittivity and permeability, where the real parts of complex permittivity (ε') and complex permeability (μ') represent the storage capability of electric and magnetic energy, and imaginary parts (ε'' and μ'') stand for the dissipation capability of these two types of energy. Owing to the absence of magnetic components in NiS_2 and MoS_2, the complex permeability can be ignored. To reveal the microwave absorption mechanism, Fig. 6 shows the complex permittivity of NiS_2/PVDF, MoS_2/PVDF and NiS_2@MoS_2/PVDF nanocomposites. It is observed that the core–shell structure has an important impact on the electromagnetic parameters. The NiS_2 nanospheres exhibit relatively high complex permittivity without external MoS_2 shells. As shown in Fig. 6a and S4,† the ε' and ε'' of 30 wt% NiS_2/PVDF decreases from 26.5 to 12.6 and from 13.5 to 9.0 with the increase of frequency, which is much higher than that of NiS_2@MoS_2/PVDF under the same filler loading. The excessive ε' and ε'' is not good for characteristic impedance match. As aforementioned, NiS_2 and NiS_2@MoS_2 nanospheres have negligible magnetic loss mechanism, therefore the incident EM wave is attenuated due to single dielectric loss mechanism. The dielectric losses are

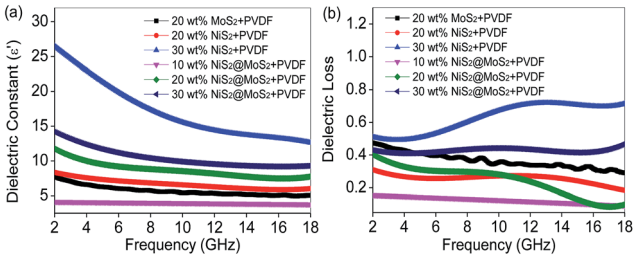

Fig. 6 Frequency dependence on (a) real part of the complex permittivity and (b) dielectric loss of samples in the frequency range 2–18 GHz.

mainly originated from the electron polarization, the ion polarization and the electric dipole polarization, *etc.* However, in the microwave range, the electron polarization and the ion polarization are insignificant, while the electric dipole polarization might be a main contributor.[24] In theory, the tangent of dielectric loss angle (δ_ε) of the material can be expressed as $\tan\delta_\varepsilon = \varepsilon''/\varepsilon'$. Fig. 6b displays that the $\tan\delta_\varepsilon$ value of 30 wt% NiS_2/PVDF is highest between 0.49 to 0.72 in frequency range of 2–18 GHz. It is unfortunate that the preferable $\tan\delta_\varepsilon$ in NiS_2/PVDF fail to endow it with excellent microwave absorption on account of the mismatched characteristic impedance. The 20 wt% NiS_2@MoS_2/PVDF shows the most enhanced EM wave absorption property while the $\tan\delta_\varepsilon$ value decreases from 0.40 to 0.09 with increasing frequency. This phenomenon indicates that the matched characteristic impedance is not the only influence factor. To illustrate the impact of core–shell structure on microwave absorption performance, we summarized the corresponding performances in Table 1. All these research has proved that the core–shell structure is beneficial for strong wave absorption ability.

In terms of the quarter-wavelength matching model, the relationship between the predicted matching thickness (t_m) and the corresponding matching frequency (f_m) can be described by the following equation:[37]

$$f_m = \frac{nc}{4t_m\sqrt{|\varepsilon_r||\mu_r|}} \quad (n = 1, 3, 5, \ldots) \tag{3}$$

Based on eqn (2), when Z_{in} is close to Z_0, the optimal absorption performance of absorber can be achieved. According to previous study,[38] when the matching thickness of the samples satisfies eqn (3), $Z = |Z_{in}/Z_0|$ is close to 1. Therefore, the minimum RL value can be obtained when the relationship between matching thickness and matching frequency of the absorbers satisfies eqn (3). As mentioned before, the minimum RL value of 20 wt% NiS_2@MoS_2/PVDF appears at 12.08 GHz under the thickness of 2.2 mm. Using eqn (3), the calculated thickness is 2.15 mm, which is very close to the theoretical thickness of 2.2 mm that is corresponding to wavelength of $\lambda/4$. It turns out that the quarter-wavelength matching theory plays an important role. Another key factor that should be considered for an excellent absorber is the attenuation constant α, which determines the attenuation properties of materials, can be determined as:[39]

$$\alpha = \frac{\sqrt{2}\pi f}{c} \times \sqrt{\mu''\varepsilon'' - \mu'\varepsilon' + \sqrt{(\mu''\varepsilon'' - \mu'\varepsilon')^2 + (\mu'\varepsilon'' + \mu''\varepsilon')^2}} \tag{4}$$

where f is the frequency of electromagnetic wave and c is the velocity of light. In general, the larger attenuation constant will result in more dielectric loss, which is beneficial to wave absorption performance. Fig. 7 gives the frequency dependence of attenuation constant α for samples. It is observed that the 30 wt% NiS_2/PVDF composites possess the largest attenuation constant among these samples in the measured frequency range while their wave absorption property is not the best. And the attenuation constant of NiS_2@MoS_2/PVDF composites with

Table 1 Comparison of the microwave absorption properties about other core–shell structural nanomaterials

Sample	Minimum RL value (dB)	Thickness (mm)	Filler loading (wt%)	Effective bandwidth (<−10 dB) (GHz)	Ref.
PPy@PANI	−34.80	2.0	50.0	4.7	33
C@C	−34.80	2.0	50.0	5.4	23
α-MoO_3@PANI	−33.70	2.0	10.0	4.0	34
Fe_3O_4@CuSilicate	−30.80	2.0	16.7	3.5	21
Fe_3O_4@SnO_2	−36.50	2.0	16.7	16.0	26
Ni@SiO_2	−40.00	1.5	70.0	3.5	28
Ni@TiO_2	−35.40	4.0	70.0	1.0	28
Cu@ZnO	−26.70	3.0	—	1.5	35
NiCu alloys	−31.13	1.5	40.0	3.0	36
$FeSn_2$@Sn@C	−28.00	3.3	50.0	7.5	24
This work	−41.05	2.2	20.0	4.4	—

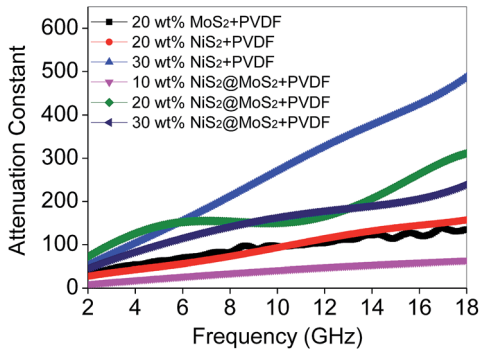

Fig. 7 Attenuation constant of various samples.

filler loading of 20 wt% is much higher than that of 10 wt% and 30 wt%. All these phenomenon has further proved that there are many factors affect the wave absorption performance.

Except for the characteristic impedance match and quarter-wavelength matching theory, it is well known that the core–shell structure of NiS_2@MoS_2 will generate multiple components and more interfaces, leading to a synergistic effect among NiS_2, MoS_2 and PVDF that is beneficial to improving wave absorption property. In the core–shell structure, surface charges tend to accumulate at the interfaces between two different dielectric media, resulting in dipole polarization. Under an external alternating EM field, the lag of induced charges that counter the increased frequency results in relaxation which is caused by the polarization of defects and transforms EM energy into heat energy.[14,40]

In addition, after coating with MoS_2 shell, the original smooth surface of NiS_2 nanospheres turns into wrinkled one, generating larger surface area. Large surface areas can provide more active sites for dissipating and scattering microwaves.[41] And according to our previous research about wave absorption performance of 3D MoS_2, it is concluded that the laminated structure is able to make the incident microwave generate multiple reflection between the different layers, which will extend the propagation path of electromagnetic wave and greatly enhance their EM wave absorption ability.[42] Furthermore, the high-curvature surfaces will lead to more remarkable interface polarization compared with spherical nanoparticles.[21]

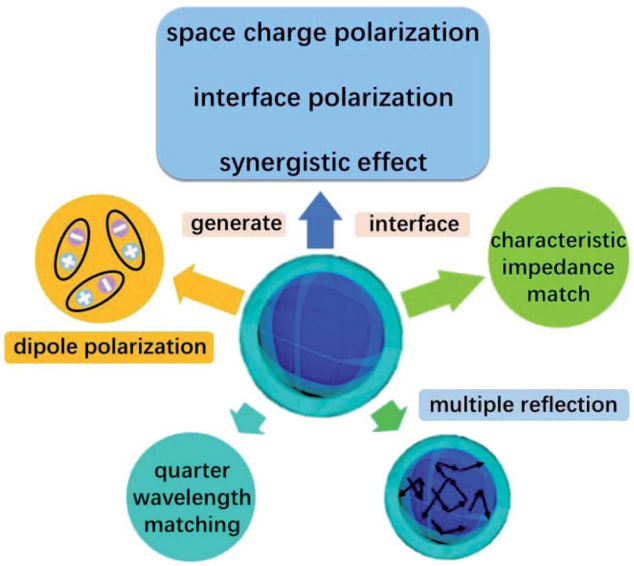

Scheme 2 The possible wave absorption mechanism of NiS_2@MoS_2/PVDF nanocomposites.

On the basis of the above discussion, the excellent microwave absorption performance of NiS_2@MoS_2/PVDF is mainly attributed to the unique core–shell structure of NiS_2@MoS_2 nanospheres which causes characteristic impedance match, synergistic effect among NiS_2, MoS_2 and PVDF, dipole polarization, interface polarization and multiple reflection. Besides, the quarter-wavelength matching theory is another important wave absorption mechanism. All these mechanism of enhanced microwave absorption have been displayed in Scheme 2 intuitively.

Experimental

All chemical reagents were purchased from Lanyi Chemical Company. And all were of analytical grade and used without further purification.

Preparation of NiS_2 nanospheres

In a typical synthesis, 0.5704 g of nickel chloride hexahydrate ($NiCl_2 \cdot 6H_2O$) and 0.128 g of sulfur powder were dispersed into

60 mL of ethylene glycol (EG) by stirring for 20 min. Then 0.96 g of polyvinyl pyrrolidone (PVP-40 000) was added. After stirring for another 30 min, the homogeneous suspension was transferred into Teflon-lined stainless steel autoclave (100 mL). After reacting in 200 °C for 12 h, the solution was cooled to room temperature. The resultant black precipitate of NiS_2 nanospheres was washed several times with distilled water and absolute ethanol and finally dried at 60 °C for 12 h for further characterization.

Preparation of core–shell NiS_2@MoS_2 nanospheres

The core–shell NiS_2@MoS_2 nanospheres was prepared *via* a facile hydrothermal method. 0.1 g synthesized NiS_2 powder was dispersed into 50 mL of de-ionized water. Then 0.08 g of sodium molybdate ($Na_2MoO_4 \cdot 2H_2O$) and 0.16 g of L-cysteine were added. After stirring for 10 min, the homogeneous suspension was transferred into Teflon-lined stainless steel autoclave (100 mL) and reacted in 200 °C for 12 h. The resultant black precipitate of NiS_2@MoS_2 nanospheres was washed several times with distilled water and absolute ethanol and finally dried at 60 °C for 12 h for further characterization. MoS_2 nanoplate has been fabricated by the same method without adding NiS_2 powder.

Characterization

XRD analyses were carried out on an X-ray diffractometer (D/MAX-1200, Rigaku Denki Co. Ltd., Japan). The XRD patterns with Cu Kα radiation ($\lambda = 1.5406$ Å) at 40 kV and 40 mA were recorded in the range of $2\theta = 5$–$80°$. Scanning electron microscope (SEM) images were achieved by a FEI Quanta 250 field-emission gun environmental scanning electron microscope at 15 kV with the samples obtained from the thick suspension dropping on the silicon slice. Field emission scanning electron microscopy (FE-SEM) on a JSM-6700F microscope. Transmission electron microscopy (TEM) and high-resolution TEM (HRTEM) investigations were carried out by a JEOL TEM-2100F microscope. X-ray photon spectroscopy was studied with a Thermo Scientific ESCALAB 250 Xi XPS system.

EM absorption measurement

The composites used for EM absorption measurement were prepared by mixing the synthesized NiS_2 nanospheres and core–shell NiS_2@MoS_2 nanospheres with polyvinylidene fluoride (PVDF) in different mass percentages, respectively. The mixtures were then pressed into cylindrical-shaped samples ($\Phi_{out} = 7.00$ mm and $\Phi_{in} = 3.04$ mm). The complex permittivity and permeability values were measured in the 2–18 GHz range with coaxial wire method by an Agilent N5230C PNA-L Network Analyzer.

Conclusions

In summary, with NiS_2 nanospheres as the cores and nucleation sites, core–shell NiS_2@MoS_2 nanocomposite have been successfully constructed through a very simple hydrothermal process. It is concluded that the NiS_2@MoS_2 nanocomposites show substantially enhanced microwave absorption properties as compared to single NiS_2 nanospheres or MoS_2 nanoplates due to this core–shell structure. With only 20 wt% filler content, the minimum reflection loss of NiS_2@MoS_2/PVDF composites reaches −41.05 dB at 12.08 GHz with a thickness of 2.2 mm and the absorption bandwidths exceeding −10 dB are 4.4 GHz. Investigations on the mechanism of microwave absorption indicate that their high performance can be caused by characteristic impedance match, synergistic effect and dielectric loss. More importantly, the excellent microwave absorption properties are highly dependent on the quarter-wavelength matching theory. This work will be helpful for the design and development of new novel microwave absorbers with multiple component and unique nanostructure.

Acknowledgements

This work was supported by the National Natural Science Foundation of China (51472012) and the Fundamental Research Funds for the Central Universities.

Notes and references

1 Y. Zhang, Y. Huang, T. Zhang, H. Chang, P. Xiao, H. Chen, Z. Huang and Y. Chen, *Adv. Mater.*, 2015, **27**, 2049–2053.
2 Z. J. Li, Z. L. Hou, W. L. Song, X. D. Liu, W. Q. Cao, X. H. Shao and M. S. Cao, *Nanoscale*, 2016, **8**, 10415–10424.
3 X. Zhang, G. Ji, W. Liu, B. Quan, X. Liang, C. Shang, Y. Cheng and Y. Du, *Nanoscale*, 2015, **7**, 12932–12942.
4 Q. Liu, Q. Cao, H. Bi, C. Liang, K. Yuan, W. She, Y. Yang and R. Che, *Adv. Mater.*, 2016, **28**, 486–490.
5 B. Zhao, B. Fan, Y. Xu, G. Shao, X. Wang, W. Zhao and R. Zhang, *ACS Appl. Mater. Interfaces*, 2015, **7**, 26217–26225.
6 H. Sun, R. Che, X. You, Y. Jiang, Z. Yang, J. Deng, L. Qiu and H. Peng, *Adv. Mater.*, 2014, **26**, 8120–8125.
7 J. Zhou, J. Qin, X. Zhang, C. Shi, E. Liu, J. Li, N. Zhao and C. He, *ACS Nano*, 2015, **9**, 3837–3848.
8 J. Xiao, L. Wan, S. Yang, F. Xiao and S. Wang, *Nano Lett.*, 2014, **14**, 831–838.
9 Y. Yan, P. Gu, S. Zheng, M. Zheng, H. Pang and H. Xue, *J. Mater. Chem. A*, 2016, **4**, 19078–19085.
10 H. Pang, X. Li, Q. Zhao, H. Xue, W. Y. Lai, Z. Hu and W. Huang, *Nano Energy*, 2017, **35**, 138–145.
11 B. Li, P. Gu, Y. Feng, G. Zhang, K. Huang, H. Xue and H. Pang, *Adv. Funct. Mater.*, 2017, **27**, 1605784.
12 J. M. Falkowski, N. M. Concannon, B. Yan and Y. Surendranath, *J. Am. Chem. Soc.*, 2015, **137**, 7978–7981.
13 J. Yang, D. Voiry, S. J. Ahn, D. Kang, A. Y. Kim, M. Chhowalla and H. S. Shin, *Angew. Chem.*, 2013, **52**, 13751–13754.
14 M. Q. Ning, M. M. Lu, J. B. Li, Z. Chen, Y. K. Dou, C. Z. Wang, F. Rehman, M. S. Cao and H. B. Jin, *Nanoscale*, 2015, **7**, 15734–15740.
15 X. J. Zhang, S. Li, S. W. Wang, Z. J. Yin, J. Q. Zhu, A. P. Guo, G. S. Wang, P. G. Yin and L. Guo, *J. Phys. Chem. C*, 2016, **120**, 22019–22027.
16 X. J. Zhang, G. S. Wang, Y. Z. Wei, L. Guo and M. S. Cao, *J. Mater. Chem. A*, 2013, **1**, 12115–12122.

17 S. He, G. S. Wang, C. Lu, J. Liu, B. Wen, H. Liu, L. Guo and M. S. Cao, *J. Mater. Chem. A*, 2013, **1**, 4685–4692.
18 M. Lu, X. Wang, W. Cao, J. Yuan and M. Cao, *Nanotechnology*, 2016, **27**, 065702.
19 X. Luo, G. S. Wang, H. Y. Guo, X. J. Zhang, W. Q. Cao, Y. Z. Wei, L. Guo and M. S. Cao, *ChemPlusChem*, 2014, **79**, 1089–1095.
20 P. Liu, Y. Huang, J. Yan, Y. Yang and Y. Zhao, *ACS Appl. Mater. Interfaces*, 2016, **8**, 5536–5546.
21 J. Xu, J. Liu, R. Che, C. Liang, M. Cao, Y. Li and Z. Liu, *Nanoscale*, 2014, **6**, 5782–5790.
22 J. Liu, J. Xu, R. Che, H. Chen, M. Liu and Z. Liu, *Chemistry*, 2013, **19**, 6746–6752.
23 R. Qiang, Y. Du, Y. Wang, N. Wang, C. Tian, J. Ma, P. Xu and X. Han, *Carbon*, 2016, **98**, 599–606.
24 X. Zhang, Y. Rao, J. Guo and G. Qin, *Carbon*, 2016, **96**, 972–979.
25 M. Yu, C. Liang, M. Liu, X. Liu, K. Yuan, H. Cao and R. Che, *J. Mater. Chem. C*, 2014, **2**, 7275–7283.
26 J. Liu, J. Cheng, R. Che, J. Xu, M. Liu and Z. Liu, *J. Phys. Chem. C*, 2013, **117**, 489–495.
27 X. Liu, X. Cui, Y. Chen, X. J. Zhang, R. Yu, G. S. Wang and H. Ma, *Carbon*, 2015, **95**, 870–878.
28 B. Zhao, G. Shao, B. Fan, W. Zhao and R. Zhang, *Phys. Chem. Chem. Phys.*, 2015, **17**, 2531–2539.
29 T. An, Y. Wang, J. Tang, W. Wei, X. Cui, A. M. Alenizi, L. Zhang and G. Zheng, *J. Mater. Chem. A*, 2016, **4**, 13439–13443.
30 Z. Yin, X. Zhang, Y. Cai, J. Chen, J. I. Wong, Y. Y. Tay, J. Chai, J. Wu, Z. Zeng, B. Zheng, H. Y. Yang and H. Zhang, *Angew. Chem.*, 2014, **53**, 12560–12565.
31 H. Zhu, J. Zhang, R. Yanzhang, M. Du, Q. Wang, G. Gao, J. Wu, G. Wu, M. Zhang, B. Liu, J. Yao and X. Zhang, *Adv. Mater.*, 2015, **27**, 4752–4759.
32 Y. Li, J. Zhang, Z. Liu, M. Liu, H. Lin and R. Che, *J. Mater. Chem. C*, 2014, **2**, 5216–5222.
33 C. Tian, Y. Du, P. Xu, R. Qiang, Y. Wang, D. Ding, J. Xue, J. Ma, H. Zhao and X. Han, *ACS Appl. Mater. Interfaces*, 2015, **7**, 20090–20099.
34 Q. Wang, Z. Lei, Y. Chen, Q. Ouyang, P. Gao, L. Qi, C. Zhu and J. Zhang, *J. Mater. Chem. A*, 2013, **1**, 11795–11801.
35 Y. F. Cheng, H. Bi, C. Wang, Q. Cao, W. Jiao and R. Che, *RSC Adv.*, 2016, **6**, 41724–41733.
36 B. Zhao, W. Zhao, G. Shao, B. Fan and R. Zhang, *ACS Appl. Mater. Interfaces*, 2015, **7**, 12951–12960.
37 H. Wang, Y. Y. Dai, D. Y. Geng, S. Ma, D. Li, J. An, J. He, W. Liu and Z. D. Zhang, *Nanoscale*, 2015, **7**, 17312–17319.
38 X. Zhang, G. Ji, W. Liu, X. Zhang, Q. Gao, Y. Li and Y. Du, *J. Mater. Chem. C*, 2016, **4**, 1860–1870.
39 X. Hong, Q. Wang, Z. Tang, W. Q. Khan, D. Zhou and T. Feng, *J. Phys. Chem. C*, 2016, **120**, 148–156.
40 T. Wu, Y. Liu, X. Zeng, T. Cui, Y. Zhao, Y. Li and G. Tong, *ACS Appl. Mater. Interfaces*, 2016, **8**, 7370–7380.
41 G. Tong, Y. Liu, T. Cui, Y. Li, Y. Zhao and J. Guan, *Appl. Phys. Lett.*, 2016, **108**, 072905.
42 M. Chen, L. Zhang, S. Duan, S. Jing, H. Jiang, M. Luo and C. Li, *Nanoscale*, 2014, **6**, 3796–3803.